Physics of the spin-orbit coupling at the surface of the model topological insulators Bi_2Se_3 and Bi_2Te_3: Theory and experiments

D. Puntel [1], F. Sammartino [1], W. Bronsch [2], S. Peli [2], F. Cilento [2], H. Ebert [3], J. Braun, [3] and F. Parmigiani [1,2,4,*]

[1] *Dipartimento di Fisica, Università degli Studi di Trieste, 34127 Trieste, Italy*

[2] *Elettra - Sincrotrone Trieste S.C.p.A., Strada Statale 14, km 163.5, 34149 Trieste, Italy*

[3] *Department Chemie, Ludwig-Maximilians-University München, Butenandtstr. 5-11, 81377 München, Germany*

[4] *International Faculty, University of Cologne, Albertus-Magnus-Platz, 50923 Cologne, Germany*

(Received 9 January 2026; accepted 3 April 2026; published 8 May 2026)

The dispersion of topological surface states in three-dimensional topological insulators (TIs) is commonly attributed to the atomic spin-orbit coupling (SOC) of the constituent elements. Whether the observable surface-state dispersion reflects this bare atomic value, or instead an effective SOC renormalized by surface–bulk hybridization, remains an open question. Here, we investigate this issue for the occupied and unoccupied surface-state dispersion in Bi_2Se_3 and Bi_2Te_3 by combining angle-resolved photoemission (ARPES) and time-resolved (tr-ARPES) at a fixed 1 ps delay time with *ab initio* one-step photoemission calculations. Comparison between experimental and calculated spectra indicates that the SOC governing the surface-state dispersion deviates from the atomic expectation, with this effect more clearly resolved in Bi_2Se_3 than in Bi_2Te_3. The calculations, which explicitly include hybridization between topological surface states and bulk-derived surface resonance states, provide a microscopic framework for this behavior. These results indicate that the spin-orbit interaction governing topological surface states is effectively shaped by surface–bulk hybridization and can vary significantly across materials.

DOI: 10.1103/mhy5-t7d1

I. INTRODUCTION

Spin-orbit coupling (SOC) in topological insulators (TIs) is responsible for the opening of an inverted bandgap between the valence and the conduction band that endows the band structure with nontrivial topology [1–5]. In the surface region separating the nontrivial insulator and the vacuum, topological arguments dictate the existence of Dirac-like states inside the gap, which are known as topological surface states [TSSs, schematized with brown lines in Fig. 1(a)] [6–8]. Since the major part of the scientific and technological interest in TIs stems from the electronic properties of the TSSs [9–15], a detailed understanding of the influence of SOC on these states is vital, as it can provide pathways to tailor the dispersion of the TSS and, therefore, the optical and transport properties of the system.

Besides the TSS, the band structure of model TIs in the vicinity of the Fermi level comprises several features, summarized in Fig. 1(a): unoccupied surface resonance states (SRSs, in dark brown) [16–18], a two-dimensional electron gas arising from surface defects (in orange) [19], and the bottom of the conduction band (in shaded yellow), which is typically populated because of unintentional electron doping of the surface [20]. A deviation of the TSS dispersion from linearity has been found to lead to the so-called *hexagonal warping* of the constant-energy surfaces (CESs) in the k_x–k_y plane [Fig. 1(b)] [21–24]. The hexagonal warping has attracted great attention because of the consequences on the out-of-plane spin polarization of the TSS [25,26] and the modification of the scattering properties arising from a larger nesting of the Fermi surface [27]. The phenomenon is most often explained employing effective models like the $\mathbf{k} \cdot \mathbf{p}$ Hamiltonian [27–29]. However, an *ab initio* characterization of the mechanism through which the SOC acts on the surface-state dispersion is still lacking.

Most interestingly, this approach was applied to the Rashba surface state of Au(111) to investigate the effect of SOC on topologically trivial surface states from an *ab initio* perspective [30]. The comparison with photoemission experiments has shown that the correct value for the Rashba splitting of these states is recovered by assuming that only the 50% of the full SOC of atomic Au acts on the surface states.

The evidence of a partial SOC transfer in the surface states of simple metals raises the question of whether this mechanism is also common to the surface states of TIs. The two cases are rather different since topological surface states retain a marked bulk character via the hybridization with the SRSs. Hence, at variance with the case of Au(111) Rashba states, the effective SOC in TIs could be mediated to the surface states via hybridization with the SRSs.

This work directly compares *ab initio* calculated angle-resolved photoelectron spectroscopy (ARPES) spectra of

*Contact author: fulvio.parmigiani@elettra.eu

Published by the American Physical Society under the terms of the Creative Commons Attribution 4.0 International license. Further distribution of this work must maintain attribution to the author(s) and the published article's title, journal citation, and DOI.

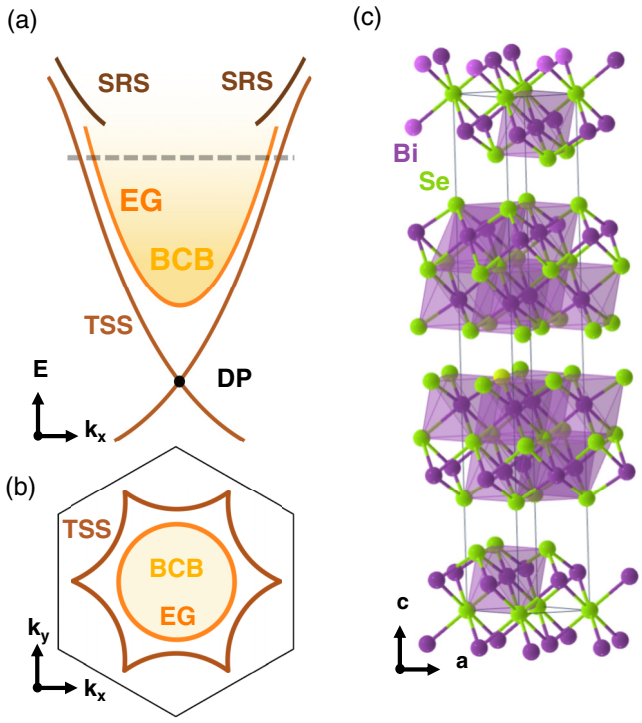


FIG. 1. (a) Scheme of the dispersion of Bi_2Se_3. The surface resonance state (SRS, dark brown), the 2D electron gas (EG, orange), the bulk conduction band (BCB, yellow), the topological surface state (TSS, brown), and the Dirac point (DP, black) are indicated. (b) CES cut at the dashed line of (a), with the features indicated accordingly. The outer black hexagon indicates the orientation of the first Brillouin zone (not scaled). (c) Conventional unit cell of Bi_2Se_3, with Bi atoms in purple and Se atoms in green. The quintuple layers are highlighted by purple tetrahedra. This panel was generated using the atomic coordinates from the Materials Project database [31,32] through the software VESTA [33].

the archetypal topological insulators Bi_2Se_3 [Fig. 1(c)] and Bi_2Te_3 with experimental ARPES and time-resolved ARPES (tr-ARPES) at a fixed 1 ps delay time spectra. The one-step photoemission calculations, which explicitly include hybridization between topological surface states and bulk-derived surface-resonance states, are used to provide a microscopic interpretation of the experimental observation, showing that such a reduction can arise naturally, softening the effective SOC and thereby significantly renormalizing the surface-state dispersion.

A crucial aspect of this problem is that the renormalization of the SOC is not uniformly reflected across the surface-state dispersion, and it must be detected also above the Fermi energy. The Dirac point in as-grown crystals lies below the Fermi level, with a position that depends on the density of substitutional defects in the bulk [20] as well as on surface aging effects [19]. This condition allows the hexagonal warping of the topological surface states to be detected by equilibrium ARPES measurements [23]. However, since the warping becomes increasingly pronounced at higher energies away from the Dirac point, tr-ARPES spectroscopy is mandatory to provide direct access to the unoccupied electronic states [24]. Unfortunately, the simultaneous implementation of conventional ARPES and tr-ARPES in a single experiment requires the use of ultrashort light pulses, which inherently broaden the spectral bandwidth. As a result, this leads to a significant reduction in both energy and momentum resolution. Under these circumstances, the comparison between calculated and measured spectra, both below and above the Fermi energy, supports a consistent phenomenological picture in which the SOC governing the surface-state dispersion is effectively softened because of hybridization with bulk-derived states. This effect is more readily resolved in Bi_2Se_3, while in Bi_2Te_3 it is partially embedded into a more complex electronic structure and stronger surface–bulk mixing.

II. MODELING THE SPIN-ORBIT COUPLING MECHANISM AT A SOLID SURFACE

In topologically trivial systems, the emergence of surface states is related to the symmetry breaking introduced by the surface itself. The surface properties are best accounted for by a realistic potential barrier, in our case of Rundgren-Malmström type [34], which includes no relativistic effect and is treated as an additional layer on top of the surface. The bulk band-structure properties, on the other hand, are determined from the fully relativistic atomic potentials in the context of the Dirac equation. To determine the coupling between the two, multiple scattering theory must be employed [35]. This coupling can be fractional, meaning that only a fraction of the relativistic properties of the atomic potentials, and thus also of the SOC, is transferred to the surface states. The physical validity of this model is demonstrated by the results obtained on the Rashba splitting of the Au(111) surface state [30] and further confirmed by the successful application of the same model to the Shockley state at the Ag/Pt(111) interface [36].

Since the existence of the TSSs directly derives from the topologically nontrivial nature of the bulk bandstructure, the bulk character of the TSSs is much more pronounced in TIs than in metal surfaces, with the consequence that the TSS extends for several layers inside the bulk. From the band-structure point of view, the bulk character is transferred to the TSS by the hybridization with SRSs [16]. These facts have two important consequences for the physics of SOC at the surface of a topological insulator. First, to determine the effect of the SOC on surface states, it is not sufficient to compute the scattering properties between the surface barrier and the atomic potentials, since this approach accounts only for physics localized entirely at the surface, which is not the case for TSS. Second, the SOC influences the surface states via a more complex mechanism than the multiple scattering between two potentials, namely the hybridization with the surface resonances, for which no analytical treatment or numerical simulation is presently available. This complexity forces one to model the SOC reduction in an effective way. The pure band-structure calculation is performed assuming the full value of the SOC for all layers of the semi-infinite bulk. The atomic potentials are then used as an input for the photoemission calculation, which includes the surface barrier and its coupling to the atomic potentials via multiple scattering. In the photoemission step of the calculation, where surface states and surface resonances are explicitly

included, the SOC of atoms within the first 20 layers of a semi-infinite stack is treated as a tunable parameter. This approach preserves the bulk band structure at full SOC, while allowing the surface-related electronic states to experience a reduced interaction, thereby modeling the effective SOC experienced by the surface electronic structure. Since Bi atoms are significantly heavier than Se atoms and dominate the SOC, the reduction is applied only to Bi sites. The underlying approach focuses on the SOC term of the first-principle Hamiltonian while leaving all other relativistic corrections unchanged [37].

III. METHODS

The electronic structure calculations were performed self-consistently in the *ab initio* framework of fully relativistic spin-density functional theory, solving the corresponding Dirac equation. The Perdew-Burke-Ernzerhof parametrization was used for the exchange and correlation potentials [38]. Furthermore, these calculations were performed for the full SOC. For the spectroscopical analysis, the spin-density-matrix formulation of the fully relativistic one-step model was employed [35,39]. The surface of the solid was represented by a Rundgren-Malmström-type potential [40], already successfully applied to the case of Bi_2Se_3 [17,41]. As this form of the surface barrier implies a z-dependent potential, the total photocurrent also includes a surface contribution that explicitly accounts for the dispersion of all the surface features. The photoemission calculations were performed for the photon energy used in the measurements (10.8 eV, see below) and for the geometry of our experimental setup. To correctly reproduce the relative intensity of the surface spectral features, the matrix elements in the surface region were calculated [30].

The measurements were performed at the Time-Resolved ARPES endstation of the T-ReX laboratory (Elettra, Trieste). The setup is based on the output of a Yb-doped fiber laser (Coherent Monaco), a fraction of which is used as a pump (at 1.2 eV or 2.4 eV obtained via second-harmonic generation). A cascade of harmonic-generation stages in BBO crystals and in Xe gas generates the ninth harmonic of the other part of the beam (10.8 eV). The incidence angle of the pump and the probe beams on the sample at normal emission is of 30°, which applies to all the measurements of this work. Further details on the setup are reported elsewhere [42]. All the measurements were performed at 110 K and with p probe polarization unless otherwise indicated.

The pump-probe measurements were performed at the fixed time delay $\Delta t \sim 1$ ps between the pump and the probe pulses, at which the population in the vicinity of the Fermi level is maximum because of the cascade relaxation mechanism of the charge carriers [43,44]. The system was excited with a p-polarized pump at a fluence of $\sim 150\ \mu J/cm^2$.

The CESs were measured with the p-polarized probe by rotating the sample in steps of 0.5° along the tilt axis (perpendicular to the analyzer slit, corresponding to k_y in our axis system for the reciprocal space) and recording an E vsk_x map for each angle. These maps are stacked together to obtain the full 3D map of the $I(E, k_x, k_y)$ photoemission intensity, which can be visualized by slicing it at constant energy.

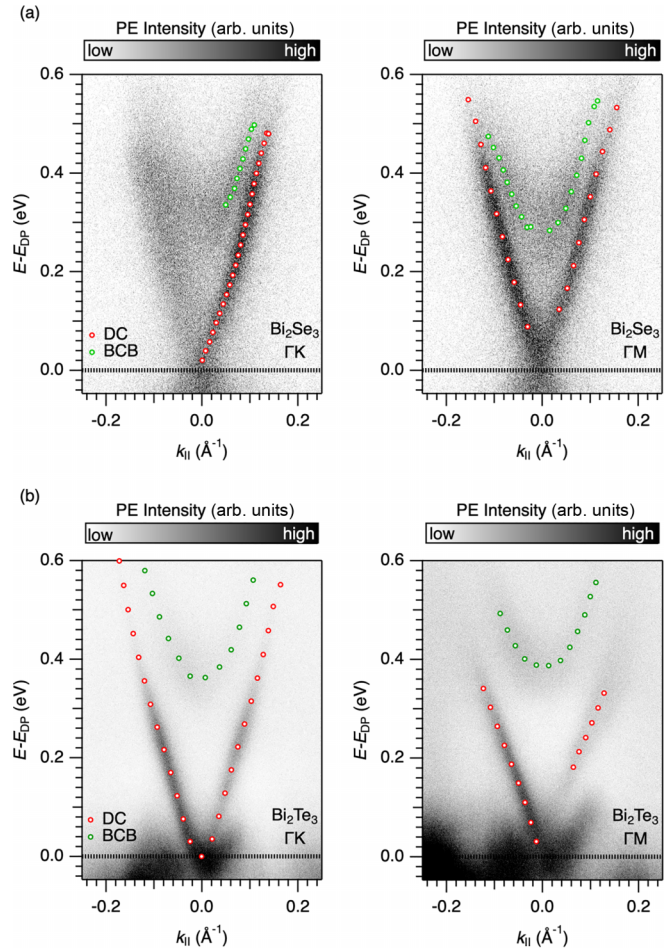


FIG. 2. ARPES intensity maps acquired along the ΓK (left panel) and ΓM (right panel) direction for (a) Bi_2Se_3 and (b) Bi_2Te_3. The red markers show the maximum intensity of the TSS as a function of energy and momentum extracted from the underlying data, and the green markers follow the dispersion of the bulk conduction band.

IV. RESULTS

Figure 2 shows our experimental ARPES results obtained with the 10.8 eV probe source for the case of Bi_2Se_3 (a) and Bi_2Te_3 (b) along the ΓK and ΓM directions, respectively. As described in more detail in the Supplemental Material [45], we applied a Gaussian filter with a width comparable to both the angular and energy resolution of the analyzer, in order to reduce noise and be able to use the Sobel algorithm to identify the intensity maxima of the maps describing the dispersions of the TSS (red markers superimposed on the as-measured photoemission intensity maps) and BCB (green markers), respectively. A common energy scale is needed to compare the experimental results with the *ab initio* calculations since, in general, the Fermi levels in the calculations and in the experiment might not coincide. The energy scales are thus aligned at the Dirac point, an unambiguous feature common to both, and referenced to the experimental Fermi energy E_F (see the Supplemental Material [45]). These results will be compared in the following with *ab initio* one-step photoemission calculations for various SOC strengths.

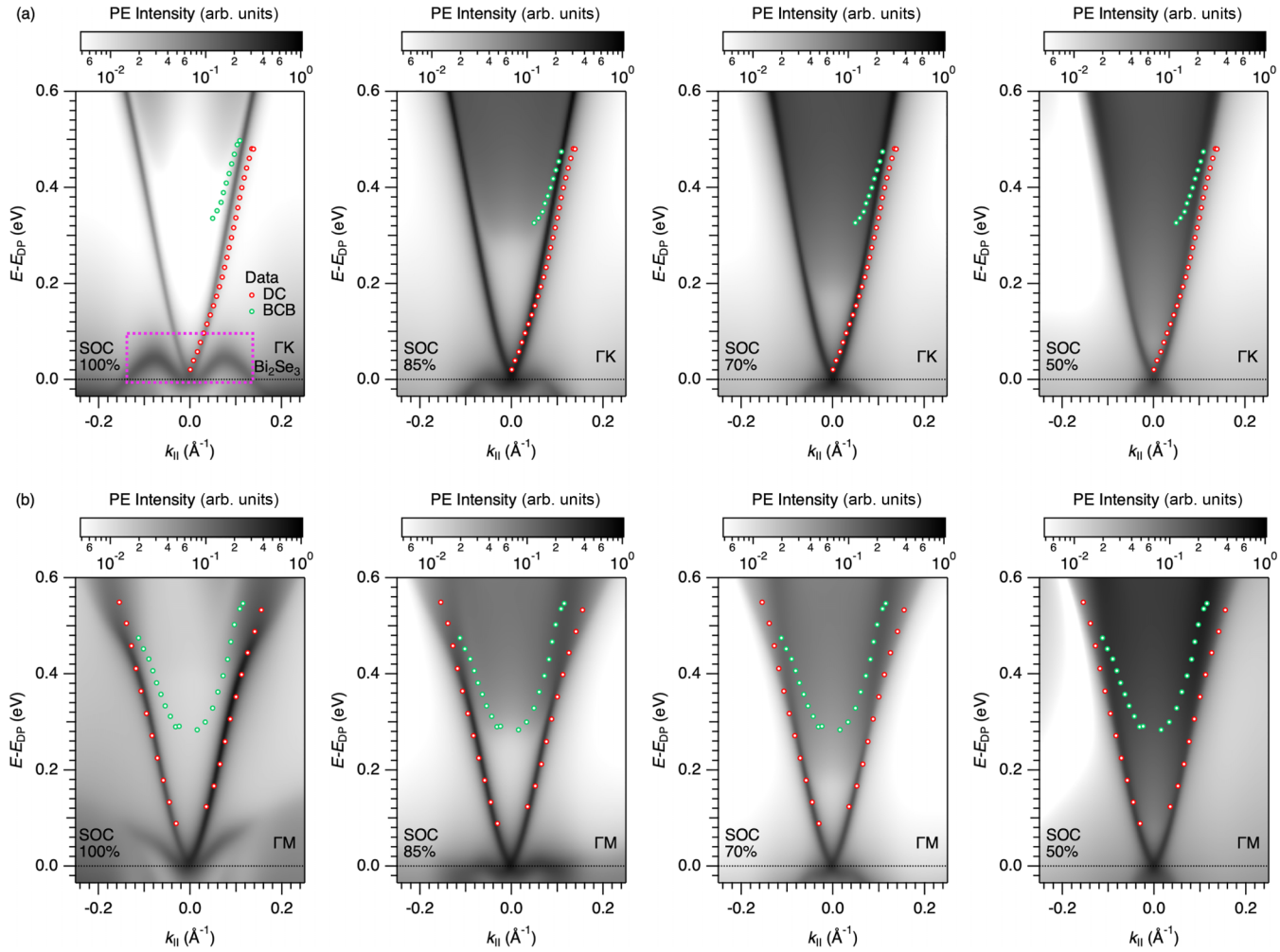


FIG. 3. *Ab initio* calculations of the Bi_2Se_3 photoemission maps for the full atomic SOC strength (100%) and reduced values of 85%, 70%, and 50% (from left to right) along the two high symmetry directions ΓK (a) and ΓM (b). The red and green markers report our experimental results shown in Fig. 2(a). The magenta box highlights the M-shaped band distortion in the vicinity of the Dirac Point, which occurs for large SOC transfer.

However, because of the finite linewidths of the surface-state bands, matrix-element effects, and the limited signal-to-noise ratio in some regions of the spectra, the experimental data do not allow a highly precise quantitative extraction of the spin-orbit coupling strength from the dispersion alone. Nevertheless, the ARPES and tr-ARPES spectra consistently indicate that the spin-orbit coupling governing the occupied and unoccupied surface-state dispersion is reduced with respect to the atomic value expected for the constituent elements. This effect is particularly clear in Bi_2Se_3 and constitutes the main experimental result of the present work.

A. *Ab initio* one-step photoemission calculations varying the SOC strength

To analyze the impact of the SOC on the TSS, we scale its strength from 100% of its full atomic value to 50%. Figure 3(a) shows the calculated photoemission maps for Bi_2Se_3 along the ΓK direction for *p*-polarized 10.8 eV photons (see also the Supplemental Material [45] for an extended energy range). The energy scale is relative to the Dirac point (DP) and ranges from slightly below the DP to ∼600 meV above it. The linearly dispersing Dirac cone displays the characteristic "V" shape above the DP, while close to it the dispersion slightly deviates from exact linearity. The part below the DP instead strongly deviates from the linear dispersion, displaying an "M"-like shape (dashed box). No population is observed between the two branches of the TSS up to ∼500 meV above the DP. From here to higher energies, a small diffuse population is visible, which we attribute to the surface projection of the bulk conduction band (BCB). As shown in the Supplemental Material [45] around ∼800 meV above the DP, a second sharp feature emerges. The position and dispersion of this feature are compatible with the SRS mentioned above [16].

Upon decreasing the SOC strength, several changes occur in the band structure. We first observe that the "M" shape of the dispersion below the DP is smeared out in favor of a monotonic dispersion. The TSS also broadens, with a width that increases with the distance from the DP. Alongside this, an increase in the BCB population is visible as a gradual change of contrast between the area enclosed by the TSS and that outside. The small intensity of the BCB with respect to the

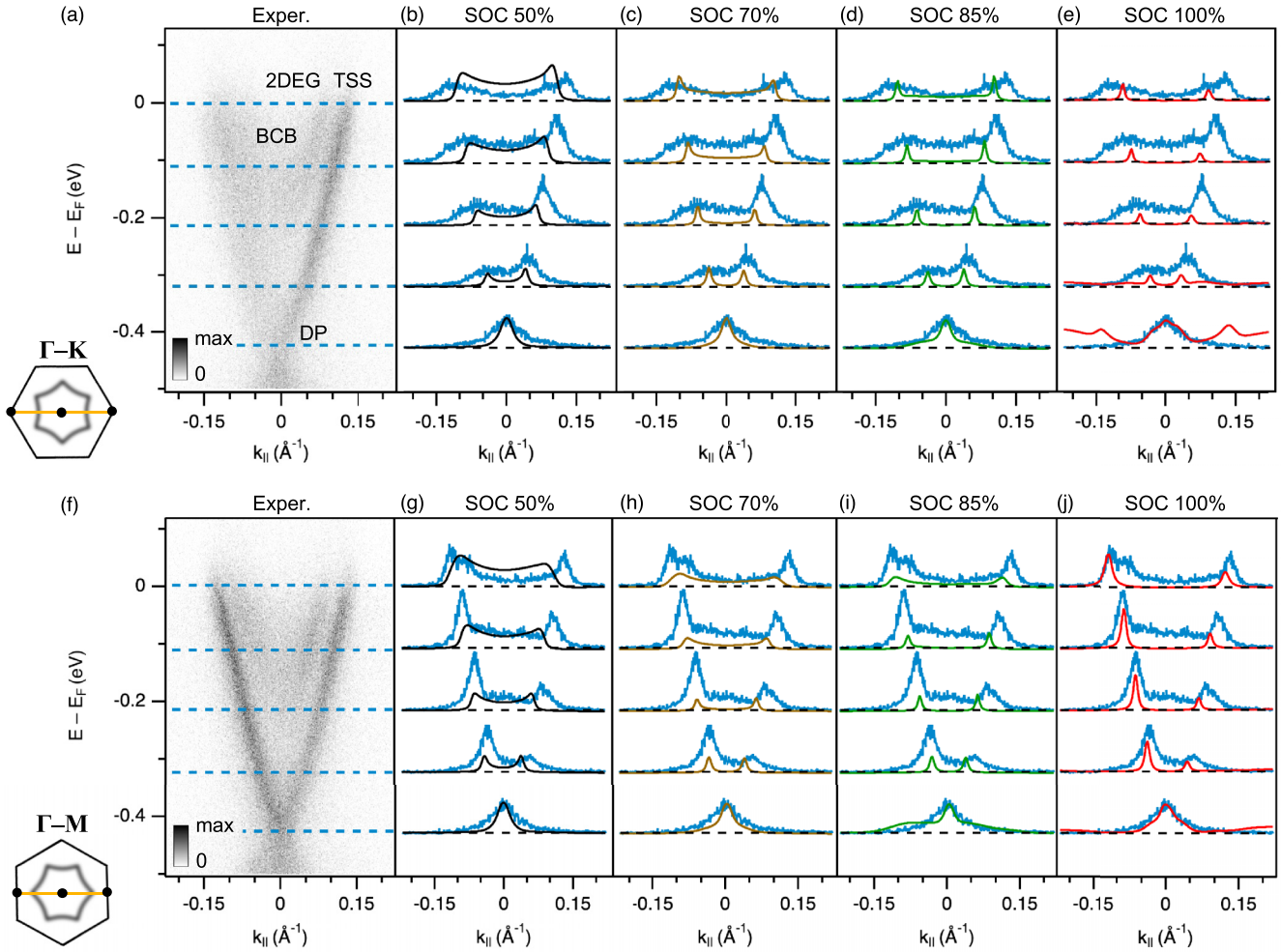


FIG. 4. (a), (f) Measured band structure of Bi_2Se_3 along the ΓK and ΓM directions, as also shown by the lower parts of (a) and (f). (b)–(e), (g), (j) MDC cuts extracted from the measurement and from the calculations with increasing SOC strength: (b), (g) 50%, (c), (h) 70%, (d), (i) 85%, and (e), (j) 100%. The cuts are extracted at the DP, at E_F and at three intermediate energies. Energies are referenced to the experimental E_F, i.e., shifting down the energy scale of the calculations by ∼410 meV.

TSS is because of a matrix element effect at this photon energy [21]. This is advantageous since it allows a larger contribution from the TSS, which is the focus of our work. At 50% SOC, however, the BCB intensity is strong and visible down to ∼100 meV above the DP. Apart from the broadening, the dispersion of both the TSS and the SRS along ΓK undergoes minimal changes, and the TSS remains linear for the whole energy region above the DP.

The dependence on the SOC of the dispersion along ΓM [Fig. 3(b)] is strikingly different. Similarly to Fig. 3(a), the TSS below the DP is bending upwards. The dispersion, while being approximately linear in the energy range 100–300 meV, strongly bends outwards around 400 meV. We stress that this downward bending along ΓM, along with the preserved linearity along ΓK, determines the warping. In the same energy range, the bands start to broaden until they are very diffuse.

B. Comparing calculations with experiment

1. Dispersion of the occupied band structure

While in Fig. 3 we superimposed the red and green markers for the experimentally determined dispersions of the TSS and BCB as a first comparison between experimental findings and theoretical predictions, in the following we will discuss a more detailed analysis of the TSS. The occupied band structure is investigated with equilibrium ARPES measurements. Figure 4 shows the comparison between the experimental and the theoretical dispersions along the two high-symmetry directions ΓK (top row) and ΓM (bottom row).

In the measured dispersion along ΓK [Fig. 4(a)], the DP is located ∼410 meV below E_F, hence signaling an n doping of the system because of aging [19,46]. This is advantageous for our investigation since it allows probing a larger part of the band structure with ARPES. The dispersion below the DP is monotonic and almost linear. Above the DP, the intensity of the two TSS branches becomes asymmetric. While the branch at negative k values (left branch) is weak and broad, the one at positive k values (right branch) is sharply defined. In between the TSS branches, the signature of a 2D electron gas (2DEG), already reported for Bi_2Se_3 [19], is visible as a narrow feature at positive k. The presence of the 2DEG confirms the aging of the surface also revealed by the relatively large distance between the DP and E_F. Also for this feature, the dispersion at negative k is weaker and broader, which makes it hard to

distinguish the TSS and the 2DEG. The contribution of the BCB is small because of the unfavorable matrix element cited above [21].

The dashed blue lines mark the energies at which the momentum distribution cuts (MDC) have been extracted, i.e., at intervals of ∼100 meV from the DP to E_F and integrated in an energy window of 10 meV. The MDCs are reported in Figs. 4(b)–4(e) in light blue and compared to the MDCs extracted from the calculated maps at variable SOC strength: (b), (g) 50%, (c), (h) 70%, (d), (i) 85%, and (e), (j) 100%.

Comparison of the dispersion in the vicinity of the DP evidences the inadequacy of the full SOC (red MDC) to account for the measured dispersion, where the TSS shows no "M"-like shape: its linearity is instead best reproduced at 50% SOC (Fig. 3). Above the DP, the MDCs show a discrepancy between experiment and calculations. In particular, the calculated MDCs seem to underestimate the cone aperture, hence predicting a higher band velocity than the one actually observed, and the discrepancy increases with the distance from the DP. This can be explained as a shortcoming of the local spin-density approach, as already reported in [30,47,48]. For the MDCs ∼100 meV and ∼200 meV below E_F, the 50% SOC seems to give a better agreement, because of the higher population of the BCB with respect to the other SOC values. The intensity measured in this region, however, is more correctly attributable to the 2DEG, since its two branches get close and because of their broadening, they partially merge. Overall, the measured relative intensity between the left and right branch of the TSS is well reproduced by all the SOC values, demonstrating that the spectroscopic calculations correctly account for the matrix element effects in our experimental geometry.

Figure 4(f) shows the measured dispersion for the ΓM direction. The intensity distribution is more symmetric than in Fig. 4(a), both for the TSS and for the 2DEG. Along this direction, also the dispersion in the vicinity of the DP for a SOC of 85% is inadequate, since the bands are bending upwards (see the bump in the MDC at $k \simeq -1$ Å^{-1}). The difference among the theoretical dispersions becomes more evident upon approaching the Fermi level. Because of the same overestimation of the band velocity commented above, the 100% SOC seems to agree better with the experimental dispersion at the Fermi level, since the effect of the warping is a detectable reduction of the band velocity along ΓM. The experimental dispersion, however, is not reflecting the strong warping experienced by the 100% SOC case (Fig. 3).

The comparison between measurements and calculations for the occupied part of the spectrum constitutes the first benchmark for the SOC fraction transferred to the TSS. The 100% SOC calculation does not satisfactorily reproduce the dispersion deduced from the experiments below the DP, for both directions. In addition, the full SOC predicts at E_F a warping larger than the one observed in the experiment. This leads to the first conclusion that the effective fraction of the SOC transferred to the surface states is smaller than the full atomic value.

2. *Dispersion of the unoccupied band structure*

Since the warping increases with the distance from the DP [24], access to larger portions of the band structure above E_F is beneficial to compare the experiments and the calculations in an energy interval where the influence of the SOC on the warping is more pronounced. Figure 5 shows the comparison between measured and calculated photoemission maps following the same arrangement of Fig. 4. The measured maps are reported as a difference between the pumped map and the equilibrium one, as customary in time-resolved ARPES measurements, to emphasize the change in the photoemission intensity. The measurement along ΓK [Fig. 5(a)] shows that the linear dispersion of the TSS is also observed above E_F. The branch at negative k values remains broad and weaker, but the one at positive k values is well distinct from the 2DEG and allows discerning that the latter disperses roughly parallel to the TSS. Accessing the dispersion above E_F is also beneficial for circumventing the unfavorable coincidence of a broad 2DEG and a small BCB contribution to the intensity. As discussed above for the region close to E_F, the parabolic dispersion of the 2DEG causes its branches to be well separated in momentum, hence allowing the attribution of the intensity detected in between to the sole BCB. This is better visible in the MDC cuts taken at ∼55 meV and ∼110 meV above E_F and shown in subsequent panels. The calculation for 50% SOC in Fig. 5(b) clearly shows an excessive intensity in correspondence with the BCB. The 70% and 85% SOC cases, Figs. 5(c) and 5(d), are instead closer to the data for the experimental dispersion, while the calculation for 100% SOC in Fig. 5(e) shows no significant BCB intensity.

The measurement along ΓM is shown in Fig. 5(f). The right branches of the TSS and of the 2DEG display a larger intensity, which is also reflected in the presence of a red signal up to higher energies. This might be because of a delay-dependent matrix element effect [49], although the depopulation of the TSS below E_F is more symmetric. The right branch clearly shows that the dispersion is deviating from linearity. Incidentally, the 2DEG population drastically decreases beyond ∼100 meV above E_F, at variance with what is observed along ΓK. The intensity of the BCB population instead follows a behavior similar to the other direction and is well reproduced for 70% and 85% SOC, as proven by the MDCs in Fig. 5(h). The magnitude of the warping agrees well with the prediction for the 85% and even 100% of the SOC. Since at higher energies the TSS is severely smeared out for lower SOC values, also the sharpness of the features is better accounted for at higher SOC values.

The inspection of the pumped E vs k maps proves that the intensity from the BCB is small compared to the TSS and the 2DEG. It also allows confirmation that the dispersion along ΓK is linear also above E_F. The dispersion along ΓM instead shows a strong warping compatible with the highest values of SOC.

3. *Comparison of constant-energy surfaces*

Observing the CESs makes it easier, with respect to the E vs k dispersion, to visualize the symmetry and the degree of deformation of the CESs to evaluate which strength of the SOC is more appropriate in describing the shape of the experimental CESs.

The result of this procedure is shown in Fig. 6(a) for the CES measured with p-polarized light. The cuts are taken at

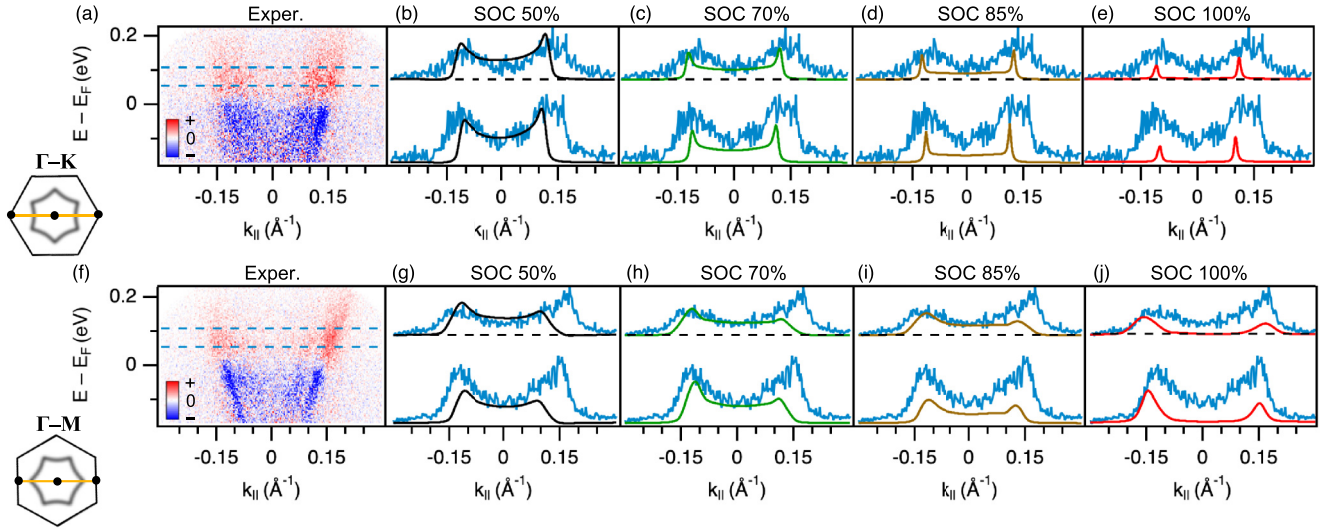


FIG. 5. Pumped counterpart of Fig. 4. Top (bottom) row refers to the ΓK (ΓM) direction of Bi_2Se_3. The experimental dispersion is reported in (a) and (g) as a difference map between the one acquired at $\Delta t = 1$ ps and the equilibrium one, to evidence the population of the band structure above E_F. (b)–(e), (g), (j) MDC cuts extracted from the measurement and from the calculations with increasing SOC strength: (b), (g) 50%, (c), (h) 70%, (d), (i) 85%, and (e), (j) 100%. The cuts are extracted 55 meV and 110 meV above E_F. Energies are referenced to the experimental E_F, i.e., shifting down the energy scale of the calculations by ∼410 meV.

five energies: at the DP, between the DP and E_F, at E_F, and at the two energies above E_F already considered in Fig. 5. The TSS contour at the DP is circular as expected from the vertex of a cone broadened by the experimental resolution. There is no intensity outside this circular area, apart from a sharp line at $k_y \sim 0.12$ Å^{-1}. This spurious intensity is probably the result of the probe beam impinging on a flake edge during the tilt angle scan. The cut at 210 meV above DP has a round shape with some larger broadening at negative k_y values, where also the photoemission intensity is larger. The TSS contour at 420 meV above DP is broader at negative k_y. At this energy, there is a clear deformation towards a hexagon. The small discontinuity at positive k_y values is likely because of a change in the probe position on the sample because of the angular motion of the latter, as suggested by the strong spurious strike of intensity commented above. The CES at 470 meV above DP shows a larger deformation of the TSS, going towards the snowflake-like shape. The case of 530 meV above the DP is analogous, with the deformation particularly visible on the right edge of the snowflake at $k_x \sim 0$ and in the top left edge. We also emphasize that the contrast between the TSS and the region inside it confirms that the BCB photoemission intensity is very weak. For a better comparison of the experimental shapes with the calculations, we superimposed on top of our experimental data and the calculations the expected snowflake distortion for Bi_2Se_3 in agreement with Kuroda *et al.* [21], who applied the phenomenological model of Fu [27] for modeling the snowflake shape of the TSS (cf. red contours in the respective panels). We want to emphasize that these curves purely serve as a guide to the eye for better readability of the figure, providing a reference size for the CES contours to better compare their changes across experiment and various SOCs, and do not attempt to relate the phenomenological description of L. Fu *et al.* [27] to our *ab initio* calculations.

The CESs were calculated for the sole SOC values of 70% [Fig. 6(b)], 85% [Fig. 6(c)], and 100% [Fig. 6(d)]. In the case of 85% and 100% SOC transfer, the "M"-shaped dispersion commented in Figs. 4(f) and 4(i) close to the DP here appears as a star-like contour of intensity, in contrast with the experimental observation presented in Fig. 6(a). A better agreement is found for 70% SOC [Fig. 6(b)]. The DP (k) is properly reproduced as a small circular area. The CES at 210 meV is still circular and becomes hexagonal only at 420 meV. Another shortcoming of this SOC value is that the warping is less severe, and thus the size of the contours at larger distance from the DP is slightly smaller than what is actually measured. Also at this SOC, the intensity asymmetry is reproduced, with a more intense CES in the negative k_y portion. We stress the fact that for both SOC values, 70% and 85%, the snowflake deformation at 470 meV and 530 meV comes along with an intense smearing of the TSS, as already commented for Fig. 5(f), with the result that the tips of the snowflake along ΓM are almost vanishing.

The comparison between the measured and the calculated CESs gives indications in agreement with what is found from the analysis of the E vs k maps. The shape of the CES close to the DP suggests a SOC value lower than 85%. On the other hand, the hexagonal deformation of the 70% SOC occurs at higher energies than the experiment suggests, and the size of the CES contour is smaller, pointing to a value of the SOC closer to 85%. The CESs also further show that the calculations correctly account for matrix element effects.

C. *Ab initio* calculations for Bi_2Te_3

After having extensively discussed the case of Bi_2Se_3 in the previous section, in the following we will focus on another member of the Bi_2X_3 family, namely Bi_2Te_3. Figure 7 shows, analogously to Fig. 3, *ab initio* photoemission calculations in comparison to the experimentally obtained dispersions of the bands (superimposed red and green markers as reported in Fig. 2). In Fig. 7(a), we show the results obtained for an

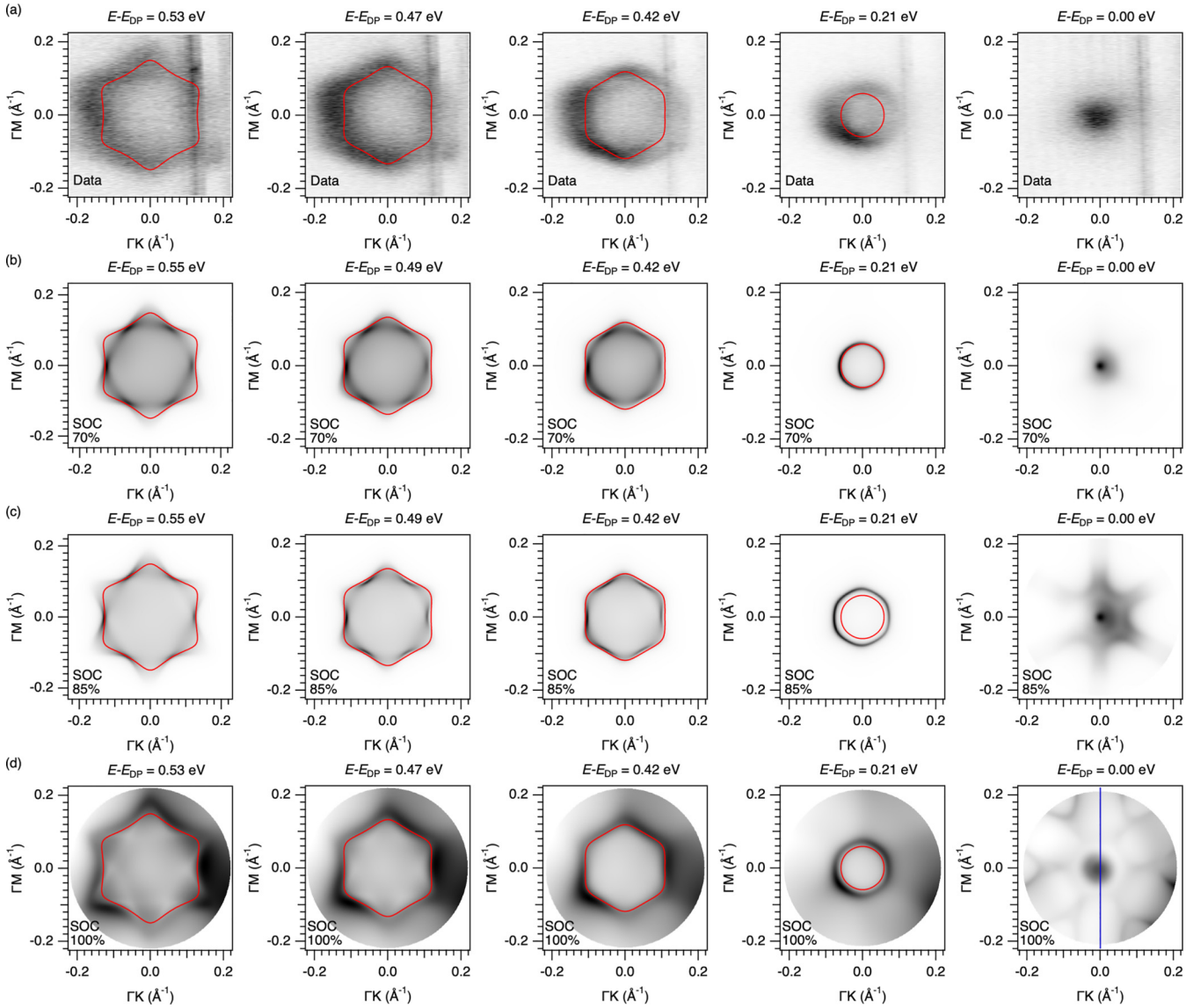


FIG. 6. Constant energy surface maps of the Bi_2Se_3 band structure at five different energies with respect to the position of the Dirac Point extracted from experimental ARPES data (a) and *ab initio* photoemission calculations assuming 70% (b), 85% (c), and 100% (d) of the full atomic SOC strength. The red line describes the expected snowflake shape according to the phenomenological model of Fu [27] using the parameters of Kuroda *et al.* [21].

assumed SOC transfer of 100%, 76%, and 48% of the full atomic value for energy-momentum cuts along the ΓK direction, while Fig. 7(b) focuses on the ΓM direction. While the dispersion of the Dirac cone along ΓK appears almost linear, a strong curvature is observed for the ΓM direction for energies 200 meV above the DP, in agreement with a strong warping reported for this material [22,27]. In the case of 100% SOC transfer, we furthermore see the SRS as a well-defined band with a parabolic dispersion and an onset of about 400 meV above the DP [17]. Reducing the SOC substantially moves the SRS to higher energies, while the DC shrinks only slightly. Comparing the experimental results with the calculations, we observe the best agreement for a full SOC transfer. Both the position of the SRS and the opening of the DC along both directions, ΓK and ΓM, agree best. Therefore, we do not find any indication for a reduced SOC transfer to the surface in the case of Bi_2Te_3. This also manifests in an overall smaller change of the band-structure features with changing SOC in the case of Bi_2Te_3 with respect to Bi_2Se_3.

V. PHENOMENOLOGICAL COMPARISON BETWEEN Bi_2Se_3 AND Bi_2Te_3

The contrast between the band structures of Bi_2Se_3 and Bi_2Te_3 can be understood by considering the balance between four main contributions: (i) spin-orbit coupling (SOC) on Bi and on the chalcogen, (ii) crystal-field splitting and Bi–chalcogen hybridization (p_z vs $p_{x/y}$), (iii) interquintuple-layer coupling affecting the k_z dispersion and the bulk band edges, and (iv) hexagonal warping and coupling to surface-resonance states. The different relative weight of these contributions in the two compounds explains both their distinct ARPES spectra and their different sensitivity to SOC strength. These

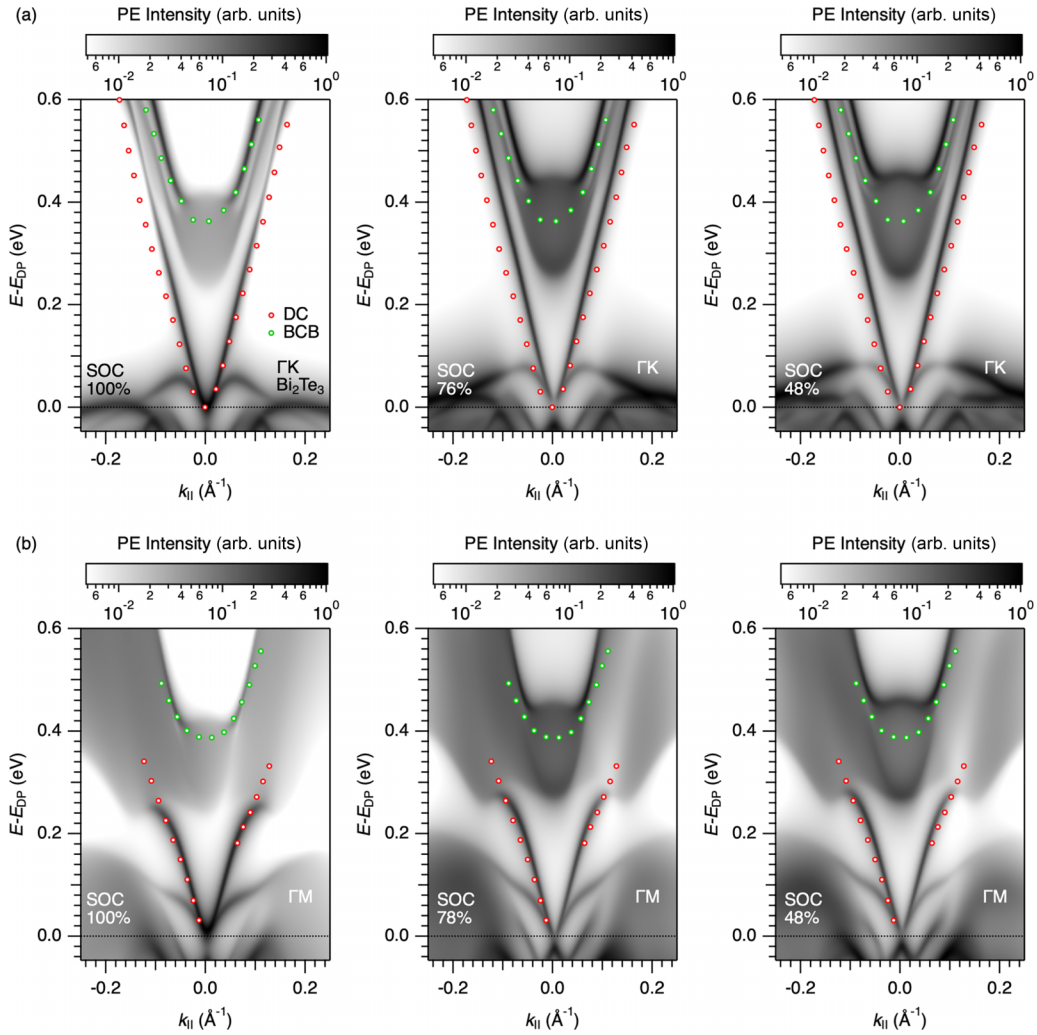


FIG. 7. *Ab initio* photoemission calculations for Bi_2Te_3 for the full atomic SOC strength (100%) and reduced values of 76% and 48% (from left to right) along the two high-symmetry directions ΓK (a) and ΓM (b). The red and green markers represent our experimental results shown in Fig. 2(b).

effects are well reflected by comparing the *ab inito* calculated ARPES spectra of Bi_2Se_3 (Fig. 3) vs Bi_2Te_3 (Fig. 7).

Bi_2Se_3 displays a comparatively clean inverted gap at Γ, where the topological surface state (TSS) is weakly perturbed by the bulk valence band. In Bi_2Te_3, the valence-band maximum lies much closer to the Dirac point, enhancing surface–bulk mixing and producing the characteristic M-shaped dispersion below the Dirac point. This difference is consistent with a stronger hexagonal warping in Bi_2Te_3, which also distorts constant-energy contours more noticeably than in Bi_2Se_3. Moreover, the proximity in energy between Te 5*p* and Bi 6*p* states leads to stronger Bi–Te hybridization and a larger $p_{x/y}$ admixture in the TSS, which modifies both the dispersion and the ARPES matrix-element pattern.

The stronger visibility of SOC tuning in Bi_2Se_3 likely arises from its proximity to the trivial topological transition. In Bi_2Te_3, SOC is intrinsically larger, but its effect on the spectral lineshape is partially obscured by the simultaneous presence of warping and surface–bulk mixing, which continue to generate M-like curvature even when the surface SOC is decreased, as clearly shown in Fig. 7. As a result, within the Bi_2X_3 family, surface SOC variations appear much more evidently in Bi_2Se_3 than in Bi_2Te_3, despite the heavier chalcogen in the latter.

VI. CONCLUSIONS

The present study combines state-of-the-art *ab initio* one-step photoemission calculations with equilibrium ARPES and tr-ARPES measurements to investigate the role of spin-orbit coupling (SOC) in shaping the topological surface states of Bi_2Se_3 and Bi_2Te_3. The experimental spectra establish that the SOC governing the surface-state dispersion deviates from the bare atomic value, with this effect more clearly resolved in Bi_2Se_3 than in Bi_2Te_3.

The calculations provide a consistent microscopic interpretation of this behavior, revealing a pronounced anisotropy in the renormalization of the dispersion, with the strongest effects occurring along the ΓM direction, where the deviation from linearity and the associated hexagonal warping become more evident, while the dispersion along ΓK remains largely unaffected. This behavior is consistent with the expectations

of $\mathbf{k} \cdot \mathbf{p}$ models and reflects the interplay between spin-orbit interaction and the underlying electronic structure.

Overall, our results establish a unified picture in which the observable properties of topological surface states are governed by the combined effect of SOC and hybridization, highlighting the importance of considering surface and bulk coupling for a realistic description of their electronic structure.

[1] C. L. Kane and E. J. Mele, Quantum spin Hall effect in graphene, Phys. Rev. Lett. **95**, 226801 (2005).

[2] L. Fu, C. L. Kane, and E. J. Mele, Topological insulators in three dimensions, Phys. Rev. Lett. **98**, 106803 (2007).

[3] J. E. Moore and L. Balents, Topological invariants of time-reversal-invariant band structures, Phys. Rev. B **75**, 121306(R) (2007).

[4] D. Hsieh, D. Qian, L. Wray, Y. Xia, Y. S. Hor, R. J. Cava, and M. Z. Hasan, A topological Dirac insulator in a quantum spin Hall phase, Nature (London) **452**, 970 (2008).

[5] M. Z. Hasan and C. L. Kane, *Colloquium*: Topological insulators, Rev. Mod. Phys. **82**, 3045 (2010).

[6] H. Zhang, C.-X. Liu, X.-L. Qi, X. Dai, Z. Fang, and S.-C. Zhang, Topological insulators in Bi_2Se_3, Bi_2Te_3 and Sb_2Te_3 with a single Dirac cone on the surface, Nat. Phys. **5**, 438 (2009).

[7] X.-L. Qi and S.-C. Zhang, Topological insulators and superconductors, Rev. Mod. Phys. **83**, 1057 (2011).

[8] A. Bansil, H. Lin, and T. Das, *Colloquium*: Topological band theory, Rev. Mod. Phys. **88**, 021004 (2016).

[9] P. Roushan, J. Seo, C. V. Parker, Y. S. Hor, D. Hsieh, D. Qian, A. Richardella, M. Z. Hasan, R. J. Cava, and A. Yazdani, Topological surface states protected from backscattering by chiral spin texture, Nature (London) **460**, 1106 (2009).

[10] D. Pesin and A. H. MacDonald, Spintronics and pseudospintronics in graphene and topological insulators, Nat. Mater. **11**, 409 (2012).

[11] B. Hamdou, J. Gooth, A. Dorn, E. Pippel, and K. Nielsch, Surface state dominated transport in topological insulator Bi_2Te_3 nanowires, Appl. Phys. Lett. **103**, 193107 (2013).

[12] A. Pandey, R. Yadav, M. Kaur, P. Singh, A. Gupta, and S. Husale, High performing flexible optoelectronic devices using thin films of topological insulator, Sci. Rep. **11**, 832 (2021).

[13] N. V. Leppenen and L. E. Golub, Nonlinear optical absorption and photocurrents in topological insulators, Phys. Rev. B **105**, 115306 (2022).

[14] M. Yang, H. Zhou, and J. Wang, Topological insulators photodetectors: Preparation, advances and application challenges, Mater. Today Commun. **33**, 104190 (2022).

[15] Y. Huang, J. D. Querales-Flores, S. W. Teitelbaum, J. Cao, T. Henighan, H. Liu, M. Jiang, G. De la Peña, V. Krapivin, J. Haber, T. Sato, M. Chollet, D. Zhu, T. Katayama, R. Power, M. Allen, C. R. Rotundu, T. P. Bailey, C. Uher, M. Trigo, *et al.*, Ultrafast measurements of mode-specific deformation potentials of Bi_2Te_3 and Bi_2Se_3, Phys. Rev. X **13**, 041050 (2023).

[16] C. Cacho, A. Crepaldi, M. Battiato, J. Braun, F. Cilento, M. Zacchigna, M. Richter, O. Heckmann, E. Springate, Y. Liu, S. Dhesi, H. Berger, P. Bugnon, K. Held, M. Grioni, H. Ebert, K. Hricovini, J. Minár, and F. Parmigiani, Momentum-resolved spin dynamics of bulk and surface excited states in the topological insulator Bi_2Se_3, Phys. Rev. Lett. **114**, 097401 (2015).

[17] C. Jozwiak, J. A. Sobota, K. Gotlieb, A. F. Kemper, C. R. Rotundu, R. J. Birgeneau, Z. Hussain, D.-H. Lee, Z.-X. Shen, and A. Lanzara, Spin-polarized surface resonances accompanying topological surface state formation, Nat. Commun. **7**, 13143 (2016).

[18] H. Hedayat, D. Bugini, H. Yi, C. Chen, X. Zhou, G. Cerullo, C. Dallera, and E. Carpene, Ultrafast evolution of bulk, surface and surface resonance states in photoexcited Bi_2Te_3, Sci. Rep. **11**, 4924 (2021).

[19] M. Bianchi, D. Guan, S. Bao, J. Mi, B. B. Iversen, P. D. King, and P. Hofmann, Coexistence of the topological state and a two-dimensional electron gas on the surface of Bi_2Se_3, Nat. Commun. **1**, 128 (2010).

[20] C. Chen, S. He, H. Weng, W. Zhang, L. Zhao, H. Liu, X. Jia, D. Mou, S. Liu, J. He, *et al.*, Robustness of topological order and formation of quantum well states in topological insulators exposed to ambient environment, Proc. Natl. Acad. Sci. USA **109**, 3694 (2012).

[21] K. Kuroda, M. Arita, K. Miyamoto, M. Ye, J. Jiang, A. Kimura, E. E. Krasovskii, E. V. Chulkov, H. Iwasawa, T. Okuda, K. Shimada, Y. Ueda, H. Namatame, and M. Taniguchi, Hexagonally deformed Fermi surface of the 3D topological insulator Bi_2Se_3, Phys. Rev. Lett. **105**, 076802 (2010).

[22] J. Sánchez-Barriga, M. R. Scholz, E. Golias, E. Rienks, D. Marchenko, A. Varykhalov, L. V. Yashina, and O. Rader, Anisotropic effect of warping on the lifetime broadening of topological surface states in angle-resolved photoemission from Bi_2Te_3, Phys. Rev. B **90**, 195413 (2014).

[23] M. Nomura, S. Souma, A. Takayama, T. Sato, T. Takahashi, K. Eto, K. Segawa, and Y. Ando, Relationship between Fermi surface warping and out-of-plane spin polarization in topological insulators: A view from spin- and angle-resolved photoemission, Phys. Rev. B **89**, 045134 (2014).

[24] M. Nurmamat, E. E. Krasovskii, Y. Ishida, K. Sumida, J. Chen, T. Yoshikawa, E. V. Chulkov, K. A. Kokh, O. E. Tereshchenko, S. Shin, and A. Kimura, Ultrafast dynamics of an unoccupied surface resonance state in $BiTe_2Se$, Phys. Rev. B **97**, 115303 (2018).

[25] S. Basak, H. Lin, L. A. Wray, S.-Y. Xu, L. Fu, M. Z. Hasan, and A. Bansil, Spin texture on the warped Dirac-cone surface states in topological insulators, Phys. Rev. B **84**, 121401(R) (2011).

[26] Y. H. Wang, D. Hsieh, D. Pilon, L. Fu, D. R. Gardner, Y. S. Lee, and N. Gedik, Observation of a warped helical spin texture in Bi_2Se_3 from circular dichroism angle-resolved photoemission spectroscopy, Phys. Rev. Lett. **107**, 207602 (2011).

[27] L. Fu, Hexagonal warping effects in the surface states of the topological insulator Bi_2Te_3, Phys. Rev. Lett. **103**, 266801 (2009).

[28] C.-X. Liu, X.-L. Qi, H. J. Zhang, X. Dai, Z. Fang, and S.-C. Zhang, Model Hamiltonian for topological insulators, Phys. Rev. B **82**, 045122 (2010).

[29] E. Frantzeskakis and M. Grioni, Anisotropy effects on Rashba and topological insulator spin-polarized surface states: A unified phenomenological description, Phys. Rev. B **84**, 155453 (2011).

[30] A. Nuber, J. Braun, F. Forster, J. Minár, F. Reinert, and H. Ebert, Surface versus bulk contributions to the Rashba splitting in surface systems, Phys. Rev. B **83**, 165401 (2011).

[31] A. Jain, S. P. Ong, G. Hautier, W. Chen, W. D. Richards, S. Dacek, S. Cholia, D. Gunter, D. Skinner, G. Ceder, and K. A. Persson, Commentary: The materials Project: A materials genome approach to accelerating materials innovation, APL Mater. **1**, 011002 (2013).

[32] The Materials Project, accessed: February 2024, https://next-gen.materialsproject.org/.

[33] K. Momma and F. Izumi, *VESTA*: A three-dimensional visualization system for electronic and structural analysis, J. Appl. Crystallogr. **41**, 653 (2008).

[34] G. Malmström and J. Rundgren, A program for calculation of the reflection and transmission of electrons through a surface potential barrier, Comput. Phys. Commun. **19**, 263 (1980).

[35] J. Braun, J. Minár, and H. Ebert, Correlation, temperature and disorder: Recent developments in the one-step description of angle-resolved photoemission, Phys. Rep. **740**, 1 (2018).

[36] A. Bendounan, K. Aït-Mansour, J. Braun, J. Minár, S. Bornemann, R. Fasel, O. Gröning, F. Sirotti, and H. Ebert, Evolution of the Rashba spin-orbit-split Shockley state on Ag/Pt(111), Phys. Rev. B **83**, 195427 (2011).

[37] H. Ebert *et al.*, The Munich SPR-KKR package, version 8.6, accessed: February 2024, https://www.ebert.cup.uni-muenchen.de/index.php/en/repository/SPRKKR/lang,en-gb/.

[38] J. P. Perdew, K. Burke, and M. Ernzerhof, Generalized gradient approximation made simple, Phys. Rev. Lett. **77**, 3865 (1996).

[39] J. Braun, K. Miyamoto, A. Kimura, T. Okuda, M. Donath, H. Ebert, and J. Minár, Exceptional behavior of *d*-like surface resonances on W(110): The one-step model in its density matrix formulation, New J. Phys. **16**, 015005 (2014).

[40] M. Grass, J. Braun, G. Borstel, R. Schneider, H. Durr, T. Fauster, and V. Dose, Unoccupied electronic states and surface barriers at Cu surfaces, J. Phys.: Condens. Matter **5**, 599 (1993).

[41] C. Datzer, A. Zumbülte, J. Braun, T. Förster, A. B. Schmidt, J. Mi, B. Iversen, P. Hofmann, J. Minár, H. Ebert, P. Krüger, M. Rohlfing, and M. Donath, Unraveling the spin structure of unoccupied states in Bi_2Se_3, Phys. Rev. B **95**, 115401 (2017).

[42] S. Peli, D. Puntel, D. Kopic, B. Sockol, F. Parmigiani, and F. Cilento, Time-resolved VUV ARPES at 10.8 eV photon energy and MHz repetition rate, J. Electron Spectrosc. Relat. Phenom. **243**, 146978 (2020).

[43] A. Crepaldi, B. Ressel, F. Cilento, M. Zacchigna, C. Grazioli, H. Berger, P. Bugnon, K. Kern, M. Grioni, and F. Parmigiani, Ultrafast photodoping and effective Fermi-Dirac distribution of the Dirac particles in Bi_2Se_3, Phys. Rev. B **86**, 205133 (2012).

[44] A. Crepaldi, F. Cilento, B. Ressel, C. Cacho, J. C. Johannsen, M. Zacchigna, H. Berger, P. Bugnon, C. Grazioli, I. C. E. Turcu, E. Springate, K. Kern, M. Grioni, and F. Parmigiani, Evidence of reduced surface electron-phonon scattering in the conduction band of Bi_2Se_3 by nonequilibrium ARPES, Phys. Rev. B **88**, 121404(R) (2013).

[45] See Supplemental Material at http://link.aps.org/supplemental/10.1103/mhy5-t7d1 for the calculations at intermediate SOC values and the procedure followed to determine the binding energy of the Dirac point.

[46] D. Hsieh, Y. Xia, D. Qian, L. Wray, J. H. Dil, F. Meier, J. Osterwalder, L. Patthey, J. G. Checkelsky, N. P. Ong, *et al.*, A tunable topological insulator in the spin helical Dirac transport regime, Nature (London) **460**, 1101 (2009).

[47] I. Aguilera, C. Friedrich, and S. Blügel, Many-body corrected tight-binding Hamiltonians for an accurate quasiparticle description of topological insulators of the Bi_2Se_3 family, Phys. Rev. B **100**, 155147 (2019).

[48] S. Ponzoni, F. Paßlack, M. Stupar, D. M. Janas, G. Zamborlini, and M. Cinchetti, Dirac bands in the topological insulator Bi_2Se_3 mapped by time-resolved momentum microscopy, Adv. Phys. Res. **2**, 2200016 (2023).

[49] F. Boschini, D. Bugini, M. Zonno, M. Michiardi, R. P. Day, E. Razzoli, B. Zwartsenberg, M. Schneider, E. H. da Silva Neto, S. dal Conte, *et al.*, Role of matrix elements in the time-resolved photoemission signal, New J. Phys. **22**, 023031 (2020).